Consumer-Grade Inertial Measurement Units Enhanced Indoor Magnetic Field Matching Positioning Scheme

Jian Kuang, Taiyu Li, Qijin Chen, Baoding Zhou, and Xiaoji Niu

***Abstract*— Magnetic field matching (MFM) positioning is one of the mainstream methods of consumer indoor positioning, which has attracted great attention from academia and industry. However, efficient methods for constructing magnetic field maps and matching positioning methods with high stability still need to be developed. This study proposes an indoor MFM positioning scheme enhanced by consumer-grade inertial measurement units that can efficiently generate a magnetic field grid map and achieve robust matching positioning, without the need to actively calibrate the magnetometer bias. When generating the magnetic field map, the proposed method employs a pedestrian positioning and orientation system to efficiently collect data by releasing individual behavioral constraints and reducing the number of control points required. Moreover, a magnetometer bias auto-calibration method, aided by the precise attitude, is proposed to simplify the data collection process. During real-time positioning, the position and attitude generated by pedestrian dead reckoning (PDR) are used to generate the differential magnetic field strength in the sensor frame; this achieves matching positioning that is independent of the magnetometer bias. Furthermore, an estimation method for the MFM position noise, based on the magnetic field gradient, is proposed to improve the accuracy of MFM/PDR integrated positioning. Several experiments were conducted to verify the feasibility and performance of the proposed scheme. Only slight differences were found between the magnetic field maps using three different smartphones, showing that the proposed scheme can efficiently generate a high-precision magnetic map. The positioning results of multiple tests conducted using eight different smartphones revealed that the proposed scheme achieves continuous and robust meter-level positioning accuracy.**

***Index Terms*— Indoor positioning, magnetic field matching (MFM), pedestrian dead reckoning (PDR), pedestrian navigation, smartphone-based positioning.**

Manuscript received 12 June 2022; revised 17 October 2022; accepted 2 November 2022. Date of publication 14 November 2022; date of current version 16 January 2023. This work was supported in part by the National Natural Science Foundation of China under Grant 41904019 and Grant 42174024, in part by the Fundamental Research Funds for the Central Universities under Grant 2042019kf0219, in part by the Shenzhen Scientific Research and Development Funding Program under Grant JCYJ20190808113603556, and in part by the Special Fund of Hubei Luojia Laboratory under Grant 220100007. The Associate Editor coordinating the review process was Dr. Chao Wang. *(Corresponding author: Qijin Chen.)*

Jian Kuang, Taiyu Li, Qijin Chen, and Xiaoji Niu are with the GNSS Research Center, Wuhan University, Wuhan, Hubei 430072, China (e-mail: kuang@whu.edu.cn; taiyuli@whu.edu.cn; chenqijin@whu.edu.cn; xjniu@whu.edu.cn).

Baoding Zhou is with the Institute of Urban Smart Transportation and Safety Maintenance, Shenzhen University, Shenzhen, Guangdong 518060, China (e-mail: bdzhou@szu.edu.cn).

Digital Object Identifier 10.1109/TIM.2022.3221754

I. Introduction

LOCATION-BASED services (LBSs) have become an indispensable part of the lives and jobs of a large number of people. Positioning technology is one of the core technologies of LBSs [1], [2]. Compared with global navigation satellite system (GNSS), which are used for outdoor environments, to date, a reliable positioning solution for indoor positioning technologies has not been developed due to the complicated nature of indoor spatial structures. This issue has continued to attract the attention of researchers in academia and industry. Many positioning methods have been developed to solve indoor positioning problems [3], such as Wi-Fi [4], Bluetooth [5], radio frequency identification (RFID) [6], fifth-generation mobile communication technology (5G) [7], ultra-wideband (UWB) [8], magnetic field matching (MFM) [9], and pedestrian dead reckoning (PDR) [10].

MFM has the advantages of ubiquity, stability, and immunity to influences from the human body [9] and is one of the mainstream indoor positioning methods for consumer users. MFM is physically feasible because the interference from artificial magnetic fields (such as those formed by reinforced concrete and cables) in an indoor environment brings stronger position distinguishability than that of the geomagnetic field. Moreover, the movement of small ferromagnetic objects (e.g., tables and chairs) will only cause changes in the magnetic field in a local area (such as a circular area with a radius of 1 m) [11] and will not have a destructive effect on MFM. Thus, MFM has great potential to provide stable and reliable high-precision indoor positioning services with zero hardware cost [9].

The two main processes in MFM are: magnetic field map generation and real-time matching positioning. When generating a magnetic field map, the correlation between the geographic coordinates and the environmental magnetic field strength (MFS) must be established [12], [13]. As determining geographic coordinates is time-consuming and labor-intensive, it is necessary to reduce the measurement accuracy of the geographic coordinates to improve the data collection efficiency. During the real-time matching positioning stage, the current position of the user is determined by calculating the similarity between the observed and reference MFSs from the magnetic field map. As a given MFS may appear in many different geographic positions, it is difficult for the point matching

method to obtain stable localization performance in the area where the differences of the MFSs are not obvious. Thus, almost all high-performance MFM algorithms essentially operate through sequence matching, similar to the gravity-aided positioning method [14].

This study proposes an indoor MFM positioning scheme that is aided by consumer-grade inertial measurement units (IMUs). The proposed scheme aims to efficiently generate a magnetic field vector grid map and achieve robust matching positioning. Moreover, users no longer need to actively calibrate the magnetometer bias, which effectively improves the applicability of the MFM solution. The major contributions of this study are given as follows.

1) Based on the self-developed pedestrian positioning and orientation system (P-POS), this article proposes a scheme for generating highly efficient and reliable magnetic field maps. An iterative method for autocalibration of magnetometer bias based on the attitude provided by P-POS is also proposed. Compared with the traditional methods, the main advantages of the proposed scheme are that it requires a smaller number of control points, does not strictly constrain the way the tester holds the sensor, the walking speed, and the shape of the walking trajectory, and can automatically calibrate the magnetometer bias.
2) This study proposes an estimation method of the positioning error of the MFM based on the MFS gradient, which can effectively improve the localization performance of the author's existing MFM algorithm independent of magnetometer bias. The algorithm can resist the damaging effects of occasional magnetic field fluctuations or the disappearance of magnetic field gradients in local areas.

The remainder of this article is organized as follows. Section II summarizes related previous works. Section III provides an overview of the proposed method. Section IV details how to generate a magnetic field vector map based on P-POS. Section V provides the detailed algorithm for PDR trajectory-based MFM. Section VI evaluates the proposed method and discusses the experimental results. Finally, we conclude this article and present future work in Section VII.

II. Related Works

A. Magnetic Field Map Data Collection

Magnetic field map construction usually involves MFS collection and location labeling. Since consumer-grade magnetometers have small performance differences and high sampling rates (e.g., 100 Hz) and magnetometer observations are not affected by attitude changes, the core of the magnetic field map construction technique is how to quickly determine the geographic coordinates corresponding to the MFS. The point-to-point manual labeling method [15] provides high-precision location labeling and is suitable for all MFM algorithms, but the work efficiency is very low and cannot be applied to large-area positioning demand scenarios.

As an alternative, a walking survey (WS) can be applied to balance the measurement accuracy and costs [10], [16], [17], [18]. The basic aim of a traditional WS is to provide reliable position estimations by imposing uniform linear motion constraints on the tester while using discrete control points (i.e., positions with known coordinates) to control the cumulative error of the position in the data processing algorithm [19]. However, for large indoor areas, a large number of nonprofessional testers need to be mobilized to complete the heavy burden of magnetic field map data collection. Furthermore, the measurement accuracy of the traditional WS approach cannot overcome the issue of control points being confused for testers walking at nonlinear trajectories and nonuniform velocities. Compared with the traditional WS method, which needs to actively label the location, the simultaneous localization and mapping (SLAM)-based mapping methods realize the magnetic field feature and location labeling without any operation by the user [20]. However, SLAM requires users to revisit the same path multiple times, which severely limits the efficiency of this method.

To further reduce costs, a magnetic field map is constructed using trajectories generated from mass users [21], called crowdsourcing. The method can be divided into active and passive. The idea of active crowdsourcing is similar to that of WS, but the data collection personnel are transformed from trained users to ordinary users [22]. Due to the complicated operation process, the accuracy of location annotation cannot be guaranteed. Passive crowdsourcing realizes the location labeling of magnetic field fingerprints by clustering the movement trajectories of mass users [23], [24]. However, due to the complexity of mass user motion trajectories and the irregular dynamics of using smartphones, the accuracy of trajectories obtained by clustering is very limited. Moreover, this method is limited by the number of users, and work efficiency cannot be guaranteed.

B. Matching Algorithm

MFM algorithms include single-point-based and sequence-based methods. Single-point-based methods, such as particle filtering (PF), use only a single magnetic field observation at a time to obtain the current user's position. The idea of PF is to set many particles to retain the possible position state of the user and uses the real-time observed MFS to determine the weights of particles, continuously replicate those particles with high weights, and finally converge to an accurate position [25]. PF achieves very good localization performance because the particle filter achieves an implicit sequence matching. Nonetheless, due to the low dimension of the magnetic field feature, PF will diverge in the region where the magnetic field signal fluctuations are gentler. Therefore, follow-up research focused on how to limit the PF divergence phenomenon [11], [26], [27], [28]. However, PF usually incurs a large computational cost to ensure positioning accuracy.

Sequence-based methods, such as dynamic time warping (DTW), exploit correlations between adjacent magnetic field features to improve positional distinguishability [29], [30]. In the DTW method, the magnetic field map stores the MFS sequences corresponding to all of the user's possible walking trajectories. The MFS observed during a period of time in the positioning phase forms another sequence, thereby

transforming the MFM into a sequence similarity calculation problem. Compared with other sequence-based methods (e.g., Smith–Waterman [31]), DTW can cope with the problem of uneven walking speed of users and has better localization performance. However, traditional DTW methods cannot cope with scenarios where users can walk on arbitrary trajectories (e.g., halls), resulting in large differences in their localization performance in different indoor areas. To solve this problem, we have proposed to use PDR to observe the user's true trajectory and generate all candidate reference MFS sequences [9]. This can be achieved by combining the relative trajectory from PDR and the grid magnetic field map in real time, thus delivering a positioning accuracy close to that of a PF. However, this method still cannot cope with the decrease in accuracy caused by the flattening phenomenon of magnetic field feature fluctuations.

At the same time, data-driven artificial intelligence methods have also been used to solve the MFM problem and were found to obtain positioning performance superior to model-based methods [32], [33]. Data-driven methods extract all possible user trajectories (i.e., different lengths, shapes, and paces) based on the magnetic field grid map and use the trained network structure to establish the mapping relationship between the magnetic field sequence and the position, which can accurately infer the user's trajectories. Data-driven methods achieve the best performance in both localization accuracy and computational efficiency in the real-time matching positioning stage. However, data-driven methods have relatively high requirements for the accuracy of the magnetic field map, and the training cost is also high (i.e., different scenarios require additional training).

C. Magnetometer Bias Calibration

The measurement accuracy of an environmental MFS is restricted by the magnetometer being used. Magnetometers induce bias, scale factor, nonorthogonal, and noise errors [34]. Compared with the combined error of 10–20 milligauss (mG) arising from other factors, magnetometer bias may cause the measurement error of an MFS to reach hundreds of mG. Thus, smartphone-based MFM positioning solutions usually only consider the magnetometer bias to reduce the complexity of the calibration procedure [9]. Ellipsoid fitting based on user-specific actions (e.g., the "∞" shape action) is a commonly used magnetometer bias calibration method. However, smartphones are prone to electromagnetic effects due to changes in working conditions, resulting in frequent changes in the magnetometer bias. Then, it is very unrealistic to require mass users to actively perform the magnetometer bias calibration procedure. Many researchers have attempted to use the differential MFS in the navigation coordinates (n-frame) to eliminate the effect of magnetometer bias [27]. However, the differential MFS in the n-frame cannot eliminate the influence of the magnetometer bias when the magnetometer's attitude fluctuates significantly. The essential reason is that magnetometer biases remain relatively stable in body coordinates (b-frame) rather than n-frame. Our previous work solved this issue by projecting the reference MFS from the n-frame to the b-frame [9]. As mentioned above, the existing MFM positioning scheme cannot completely omit the procedure of actively calibrating the magnetometer bias, which seriously limits the progress of magnetic field positioning for solving indoor positioning problems.

III. Overview of the Proposed Method

For consumer-grade IMUs, the position drift of the pure inertial navigation system (INS) quickly reaches several meters (within a few seconds); this is detrimental to the needs of practical applications. Thus, it is necessary to extract the constraint information formed by the pedestrian motion law to improve the relative positioning ability of the INS. Based on the periodical footsteps of pedestrians, a high-precision P-POS consisting of a foot-mounted IMU and a built-in smartphone IMU [35] can be employed to efficiently collect the magnetic field map data. Moreover, the speed constraint observations can be constructed to control the speed error of the built-in IMU of the smartphone in the online positioning phase; this is termed the PDR algorithm [10]. The stability and positioning accuracy of an MFM can be improved by changing the relative position and attitude of the PDR. In general, consumer-grade IMUs play indispensable roles as auxiliary means in smartphone-based indoor MFM positioning schemes.

Fig. 1 shows the flow of an MFM positioning scheme based on consumer-grade IMUs. In the magnetic field map generation stage, the foot-mounted INS (Foot-INS) and sparse control points provide stable, high-precision position information, which is used to modify the positioning results of the smartphone built-in IMU, thereby forming a high-precision P-POS for the smartphone. To tackle the issue of frequent changes in the magnetometer bias, here, an automatic calibration algorithm based on high-precision attitude information is proposed. More generally, rasterization and linearization processing methods are proposed to reduce the workload of data collection while ensuring measurement accuracy.

In the online matching positioning phase, this study proposes using the relative position and attitude from the INS-based PDR algorithm to correlate the observed MFS, thus forming a magnetic field profile (MFP). The profile can then be used to generate the differential MFP in the b-frame, which eliminates the influence of the magnetometer bias. To reflect the accuracy level of the position output by MFM, here, a position noise estimation method is proposed based on the magnetic field gradient. This method is designed to improve the accuracy of MFM/PDR integrated positioning. More importantly, the scale factor of the step-length estimation model can be estimated accurately by the filter, further improving the accuracies of the relative trajectory and current position predictions. Finally, the proposed MFM/PDR combined positioning method will reach a state of mutual assistance and mutual promotion.

IV. Magnetic Field Map Generation Stage

The construction methods for magnetic field maps differ depending on the application requirements; this essentially comprises a compromise between measurement accuracy and cost. Therefore, for the application and promotion of MFM positioning schemes, it is important to develop an economical

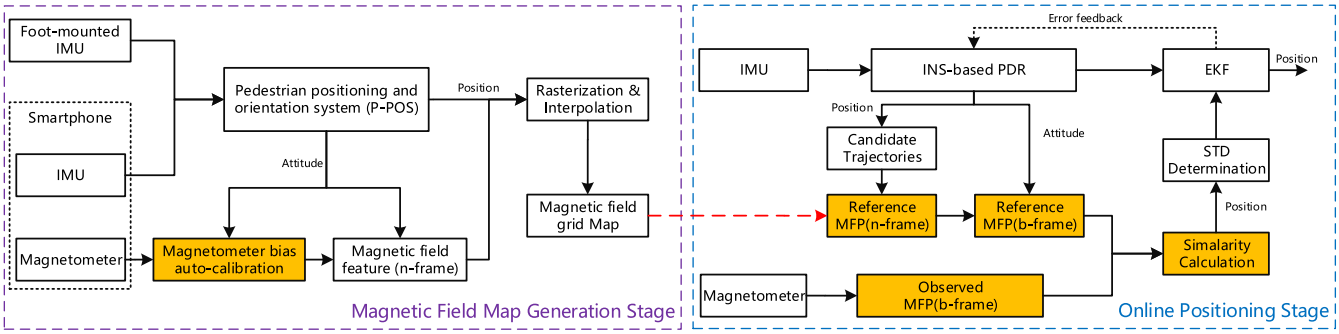

Fig. 1. Block diagram of the consumer IMU-based MFM positioning scheme.

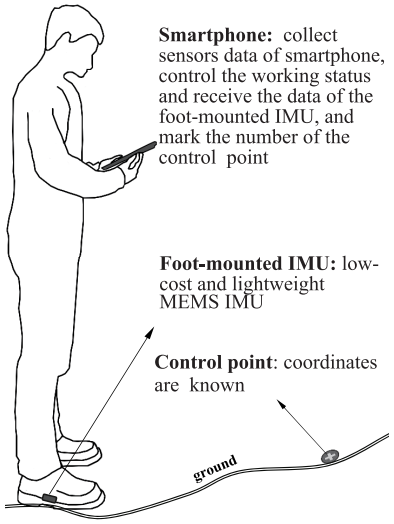

Fig. 2. Structure of P-POS [35].

method that generates highly efficient and precise magnetic field maps.

A. Determining the Position and Attitude of the Magnetometer

Considering the requirements of consumer indoor positioning accuracy (approximately 1–3 m) and the uniform distribution of magnetic fields in most areas, here, a WS method combined with linear interpolation is proposed to generate a high-resolution magnetic field map [12], [19]. To reduce the workload of data collection without any loss of resolution for the resulting MFS, an "S" shape is proposed to collect magnetic field data; the distance between adjacent trajectories should be $\leq$ 2.0 m.

In the proposed data processing phase, the P-POS is used to determine the position and attitude of the smartphone. Fig. 2 shows the structure of the P-POS, including a smartphone, a foot-mounted IMU, and a small number of control points. The basic principle of P-POS is given as follows. The Foot-INS (i.e., foot-mounted IMU-based INS integrated with a zero-velocity update technique) combined with a small number of control points (i.e., the coordinate known points) is used to provide a continuous high-precision position. The precise positioning of the Foot-INS is integrated with the smartphone's built-in IMU-based INS to accurately estimate position and attitude, similar to GNSS/INS integration in outside environments. The lever arm between the smartphone built-in INS and the Foot-INS is solved by capturing a specific phase of the gait cycle that has a consistent relative pose between a pedestrian's wrist and heel. The detailed algorithm of P-POS can be found in [35]. Test results show that P-POS can provide decimeter-level positioning and degree-level attitude when the distance between adjacent control points is 50 m. In this study, a handheld smartphone replaced the back-mounted IMU in P-POS, thus requiring the testers to minimize the relative distance between the phone and the body (e.g., the waist) during the data collection process.

The traditional WS method achieves efficient data collection tasks by restricting personal behaviors (such as walking in a straight line at a uniform speed and keeping the smartphone oriented parallel to the walking direction of pedestrian) [18]. However, this practice is only suitable for professionals in small indoor scenarios. When considering the indoor magnetic field map data collection with a citywide, the complex indoor environment and the nonprofessional testers will make this practice of limiting individual behavior impossible to implement. P-POS releases individual behavioral constraints by observing the dynamics of the user's feet and wrists using footworn and handheld IMUs. In addition, with the support of powerful relative positioning capabilities, P-POS requires only a very small number of control points. Thus, even for nonprofessional testers in complex indoor environments, the efficiency of data collection can be greatly improved and the measurement of decimeter-level position and degree-level attitude can be achieved.

B. User-Free Magnetometer Bias Calibration

As smartphones are highly integrated electronic devices, it is very easy for them to generate electromagnetic interference, thus changing the magnetometer bias. To eliminate this effect, testers are frequently required to conduct specific actions (i.e., "∞" movement) to calibrate the magnetometer bias before collecting magnetic field data [36]. However, in the absence of supervision, testers will refuse to complete this specific calibration action. Therefore, an automatic calibration method for magnetometer bias is necessary to ensure the quality of the magnetic field map.

The Earth's magnetic field comprises the main part of an ordinary indoor environmental magnetic field, so it is safe to assume that the mean value of the magnetic field interference in a local area is zero. Our published work provides ample validation of this hypothesis [37]. In other words, the average value of the magnetic field vector observed by the test track can be considered to be equal to the geomagnetic field vector. The magnetometer bias does not change over a short period (e.g., 10 min) [34], so the relationship between the observed magnetic field and geomagnetic field vectors can be described as

$$\boldsymbol{M}^n \approx \frac{1}{k}\sum_{i=1}^{k} \boldsymbol{C}_{b,i}^n \left(\tilde{\boldsymbol{M}}_i^b - \boldsymbol{b}_m\right) \tag{1}$$

where $\boldsymbol{M}^n$ is the true magnetic field vector, which can be obtained by querying the International Geomagnetic Reference Field (IGRF) [38]; $\tilde{\boldsymbol{M}}_i^b$ is the observation of the magnetometer; $\boldsymbol{b}_m$ is the bias of the magnetometer; $\boldsymbol{C}_{b,i}^n$ is the directional cosine matrix from the b-frame to the n-frame, which comes from P-POS; and k is the number of magnetometer measurements.

The coordinates of the control points used by P-POS are usually defined in a local horizontal coordinate system. This means that the output absolute heading is not equal to the absolute heading and that the horizontal component of the magnetic field cannot be accurately obtained. Therefore, in addition to the vertical component of the MFS, this study proposes an iterative method for solving the horizontal magnetic field intensity component as follows.

1) The initial value of the magnetic field vector M_0^n can be obtained by

$$\boldsymbol{M}_0^n \approx \frac{1}{k}\sum_{i=1}^{k} \boldsymbol{C}_{b,i}^n \tilde{\boldsymbol{M}}_i^b. \tag{2}$$

2) Based on the assumption that the magnetometer bias does not change over a short time period [34], the magnetometer bias can then be recalculated as follows:

$$\boldsymbol{b}_{m,1} \approx \frac{1}{k}\sum_{i=1}^{k} \left(\tilde{\boldsymbol{M}}_i^b - \boldsymbol{C}_{n,i}^b \boldsymbol{M}_0^n\right) \tag{3}$$

where "1" is the number of iterations.

3) By substituting $\boldsymbol{b}_{m,1}$ into 1, it is possible to calculate the magnetic field vector $\boldsymbol{M}_1^n$.

4) Steps 2) and 3) can then be repeated until the following equation is satisfied:

$$\left\|\boldsymbol{M}_{i-1}^n - \boldsymbol{M}_i^n\right\| < \gamma \tag{4}$$

where γ is the threshold for determining the convergence of the algorithm and i is the number of iterations. Then, the 3-D MFS of a single position in the n-frame can be described as

$$\hat{\boldsymbol{M}}_i^n = \boldsymbol{C}_{b,i}^n \left(\tilde{\boldsymbol{M}}_i^b - \hat{\boldsymbol{b}}_m\right) \tag{5}$$

where $\hat{\boldsymbol{M}}_i^n$ is the estimated magnetic field vector and $\hat{\boldsymbol{b}}_m$ is the calibrated magnetometer bias.

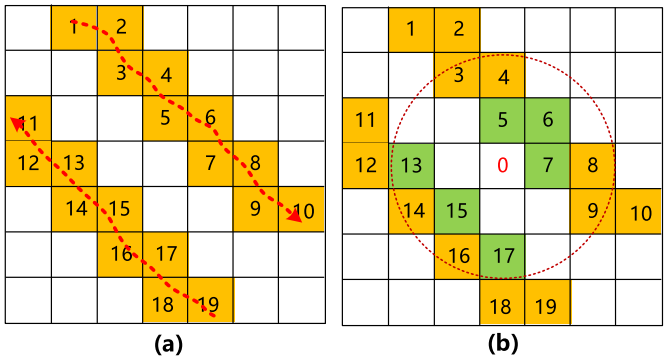

Fig. 3. Generation process of grid magnetic field map. (a) Rasterization. (b) Linear interpolation.

C. Grid Map Generation

The high sampling rates of magnetometers (e.g., 100 Hz) and the uneven distribution of the reference trajectories result in some areas being collected multiple times, while some areas are not covered. To solve this problem, the interpolation methods, such as the Gaussian model, Kriging, and bilinear, are used to fill in the magnetic field features of the uncollected area [39]. As the magnetic field features are evenly distributed in most areas of the indoor environment, the influence of local strong magnetic interference is only about a 1-m radius. Furthermore, the sequence-based MFM algorithm used in this study can better adapt to the effects of accidental magnetic field disturbances. Therefore, compared with better interpolation methods such as the Gaussian model and Kriging, the linear interpolation method is sufficient to meet the low-precision positioning needs of mass users (e.g., about 1 m). The specific generation method of the grid magnetic field map is given as follows.

Rasterization: First, a minimum rectangle is generated according to the estimated coordinates of the reference trajectories. The rectangle is then divided into grids of the same size (e.g., with a side length of 0.3 m). Second, the observed MFSs are allocated to these grids according to the estimated coordinates, and the MFS in the same grid is averaged. In Fig. 3(a), the red dotted line is the test track and the orange square is the valid grid.

Linear Interpolation: First, the position coordinates of the grid to be interpolated are determined [e.g., grid No. 0 in Fig. 3(b)]. The search radius of the effective grid is then set (e.g., 1 m). Second, traverses are conducted in eight directions (east, south, west, north, northwest, northeast, southeast, and southwest) of grid No. 0. If a grid with a valid MFS is detected, it will return true (such as grids numbered 5, 6, 7, 13, 15, and 17). Third, valid grids are used to obtain the magnetic field features of grid No. 0 by linear interpolation. The linear interpolation formula can be expressed as follows:

$$\boldsymbol{M}_0^n = \frac{\boldsymbol{M}_{5,17}^n + \boldsymbol{M}_{6,15}^n + \boldsymbol{M}_{7,13}^n}{3} \tag{6}$$

where $\boldsymbol{M}_{i,j}^n = (d_{i-0}\boldsymbol{M}_j^n + d_{j-0}\boldsymbol{M}_i^n / d_{i-0} + d_{j-0})$, $\boldsymbol{M}_i^n$ is the MFS of the ith grid and $d_{i-0} = ((n_i - n_0) + (e_i - e_0))^{1/2}$ is the distance between the ith grid and the 0th grid.

Finally, a uniformly distributed magnetic field map can be obtained. The data format of the ith grid is given as follows:

$$\mathrm{MFF}_i = \left\{ \boldsymbol{r}_i^n \quad \boldsymbol{M}_i^n \right\}. \tag{7}$$

V. Real-Time Positioning Stage

Due to the low dimensionality of a magnetic field at a single position (e.g., three dimensions at most), PDR is commonly used to improve the positioning performance of MFM for pedestrians. PDR can effectively reduce the search area of MFM by predicting the current position. The combined features of the MFS time series and the relative trajectory generated by the PDR can also effectively improve position discrimination.

A. INS-Based PDR

In the step-model-based PDR method, the position error is separated from the sensor error. Thus, the sensor error cannot be estimated by correcting the position error. In addition, the dynamic information between the two steps cannot be obtained because the output frequency of this method is low (e.g., 2 Hz). This study, therefore, employs an INS-based PDR method to generate a relative trajectory to improve the positioning performance of the MFM method. As the built-in inertial sensors in smartphones are low quality, small error corrections (e.g., Earth's rotation) will be ignored because they cannot bring significant performance improvements. The simplified INS mechanization is given by [10], [40]

$$\begin{cases} \boldsymbol{r}_k^n = \boldsymbol{r}_{k-1}^n + \boldsymbol{v}_k^n \Delta t_k \\ \boldsymbol{v}_k^n = \boldsymbol{v}_{k-1}^n + \boldsymbol{C}_{b,k}^n \left(\Delta \boldsymbol{v}_k^b \right) - \boldsymbol{g}^n \Delta t_k \\ \boldsymbol{C}_{b,k}^n = \boldsymbol{C}_{b,k-1}^n \left[\boldsymbol{I} + \Delta \boldsymbol{\theta}_k^b \times \right] \end{cases} \tag{8}$$

where $\boldsymbol{r}^n$ and $\boldsymbol{v}^n$ are the position and velocity vectors in the n-frame, respectively; $\boldsymbol{C}_b^n$ is the transformation matrix from the b-frame to the n-frame; $\boldsymbol{g}^n = [0, \ 0, \ -g]^T$ is the Earth's gravity vector; $\Delta \boldsymbol{v}_k^b = (\tilde{\boldsymbol{f}}_k^b - \boldsymbol{b}_{f,k}) \Delta t_k$ is the velocity increment in the b-frame; $\tilde{\boldsymbol{f}}^b$ and $\boldsymbol{b}_f$ are the acceleration and bias of the accelerometer, respectively; $\Delta \boldsymbol{\theta}_k^b = (\tilde{\boldsymbol{\omega}}_k^b - \boldsymbol{b}_{g,k}) \Delta t_k$ is the angle increment in the b-frame; $\tilde{\boldsymbol{\omega}}^b$ and $\boldsymbol{b}_g$ are the angle rate and bias of the gyroscope, respectively; $\Delta t = t_k - t_{k-1}$ is the time interval between the $(k-1)$th and kth epochs; and "$\times$" is the cross-product form of a vector.

The navigation performance of the INS mechanization algorithm depends substantially on sensor accuracy. Pedestrian motion characteristics are used to slow down the cumulative speed of the position errors for meeting the needs of practical applications. This study uses the error-state Kalman filter to fuse the INS and pedestrian motion constraints. The 16-D error-state variables are defined as

$$\delta \boldsymbol{x} = \left[\delta \boldsymbol{r}^n \quad \delta \boldsymbol{v}^n \quad \boldsymbol{\phi} \quad \delta \boldsymbol{b}_g \ \delta \boldsymbol{b}_a \quad \delta s \right]^T \tag{9}$$

where $\delta \boldsymbol{r}^n$ and $\delta \boldsymbol{v}^n$ are the position and velocity error vectors in the n-frame, respectively; $\boldsymbol{\phi}$ is the attitude error vector; $\delta \boldsymbol{b}_g$ and $\delta \boldsymbol{b}_a$ are the bias error vectors of the gyroscope and accelerometer, respectively; and δs is the scale error of the step length. As the empirical model cannot adapt to different users, the step scale factor is used as an estimation variable; the MFM result is used to estimate it effectively.

The discrete linearization of the system error model can be expressed as follows:

$$\begin{cases} \delta \boldsymbol{x}_{k,k-1} = \boldsymbol{\Phi}_{k,k-1} \delta \boldsymbol{x}_{k-1,k-1} + \boldsymbol{w}_k \\ \delta \boldsymbol{z}_k = \boldsymbol{H}_k \delta \boldsymbol{x}_{k,k-1} + \boldsymbol{v}_k \end{cases} \tag{10}$$

where the subscripts $k-1$ and k represent the epoch, $\delta \boldsymbol{z}$ is the measurement misclosure vector, $\boldsymbol{H}$ is the design matrix, $\boldsymbol{w}$ is the process noise, $\boldsymbol{v}$ is the measurement noise, and $\boldsymbol{\Phi}$ is the 16×16 state transition matrix [9] as follows:

$$\boldsymbol{\Phi}_{k,k-1} = \begin{bmatrix} \boldsymbol{I}_3 & \boldsymbol{I}_3 \Delta t & \boldsymbol{0}_3 & \boldsymbol{0}_3 & \boldsymbol{0}_3 & \boldsymbol{0}_{3\times 1} \\ \boldsymbol{0}_3 & \boldsymbol{I}_3 & \left(\boldsymbol{f}_k^n \times \right) \Delta t & \boldsymbol{0}_3 & \boldsymbol{C}_{b,k}^n \Delta t & \boldsymbol{0}_{3\times 1} \\ \boldsymbol{0}_3 & \boldsymbol{0}_3 & \boldsymbol{I}_3 & -\boldsymbol{C}_{b,k}^n \Delta t & \boldsymbol{0}_3 & \boldsymbol{0}_{3\times 1} \\ \boldsymbol{0}_3 & \boldsymbol{0}_3 & \boldsymbol{0}_3 & \boldsymbol{I}_3 & \boldsymbol{0}_3 & \boldsymbol{0}_{3\times 1} \\ \boldsymbol{0}_3 & \boldsymbol{0}_3 & \boldsymbol{0}_3 & \boldsymbol{0}_3 & \boldsymbol{I}_3 & \boldsymbol{0}_{3\times 1} \\ \boldsymbol{0}_{1\times 3} & \boldsymbol{0}_{1\times 3} & \boldsymbol{0}_{1\times 3} & \boldsymbol{0}_{1\times 3} & \boldsymbol{0}_{1\times 3} & 1 \end{bmatrix} \tag{11}$$

where $\boldsymbol{0}_3$ and $\boldsymbol{I}_3$ are the 3×3 zero matrix and identity matrix, respectively, and $\boldsymbol{0}_{1\times 3}$ and $\boldsymbol{0}_{3\times 1}$ are the 1×3 and 3×1 zero matrices, respectively. When the observations are valid, the following methods can be used to update the state variables and their corresponding covariance values:

$$\delta \hat{\boldsymbol{x}}_k = \delta \hat{\boldsymbol{x}}_{k,k-1} + \boldsymbol{K}_k \left(\delta \boldsymbol{z}_k - \boldsymbol{H}_k \hat{\boldsymbol{x}}_{k,k-1} \right) \tag{12}$$

$$\boldsymbol{P}_k = (\boldsymbol{I} - \boldsymbol{K}_k \boldsymbol{H}_k) \boldsymbol{P}_{k,k-1} (\boldsymbol{I} - \boldsymbol{K}_k \boldsymbol{H}_k)^T + \boldsymbol{K}_k \boldsymbol{R}_k \boldsymbol{K}_k^T \tag{13}$$

$$\boldsymbol{K}_k = \boldsymbol{P}_{k,k-1} \boldsymbol{H}_k^T \left(\boldsymbol{H}_k \boldsymbol{P}_{k,k-1} \boldsymbol{H}_k^T + \boldsymbol{R}_k \right)^{-1}. \tag{14}$$

The pseudo-velocity observations formed by pedestrian motion constraints can be described as [10]

$$\delta \boldsymbol{z}_v = \hat{\boldsymbol{v}}^b - \tilde{\boldsymbol{v}}^b = \boldsymbol{C}_n^b \delta \boldsymbol{v}^n - \boldsymbol{C}_n^b \left(\boldsymbol{v}^n \times \right) \boldsymbol{\psi} - \tilde{\boldsymbol{v}}^b \delta s + \boldsymbol{n}_v \tag{15}$$

where $\hat{\boldsymbol{v}}^b$ and $\boldsymbol{v}^n$ are the velocities of the INS in the b-frame and n-frame, respectively; n_v is the observation noise; and $\tilde{\boldsymbol{v}}^b$ are pseudo-velocity observations in the b-frame. When the state of a pedestrian is determined to be standing, $\tilde{\boldsymbol{v}}^b$ can be reasonably considered to be zero. When a user is walking forward regularly, the lateral and vertical velocities of the body coordinate system should be zero, and the walking velocity can be estimated by their step detection and a previously published empirical step-length estimation model [10]. $\tilde{\boldsymbol{v}}^b$ can be described as follows:

$$\tilde{\boldsymbol{v}}^b = \begin{bmatrix} \dfrac{s \cdot L}{t_k - t_{k-1}} & 0 & 0 \end{bmatrix}^T \tag{16}$$

where L is the step length from the empirical model, s is the scale of the estimated step length, and t_k and t_{k-1} are the times of the kth and $(k-1)$th steps, respectively.

B. MFM Algorithm

In the proposed method, the MFS time series and the corresponding relative positions from the PDR are correlated with form a combined feature, called the MFP. Changes in the relative spatial relationship (such as direction and distance) between two adjacent MFSs are preserved, which improves the MFP's position discrimination.

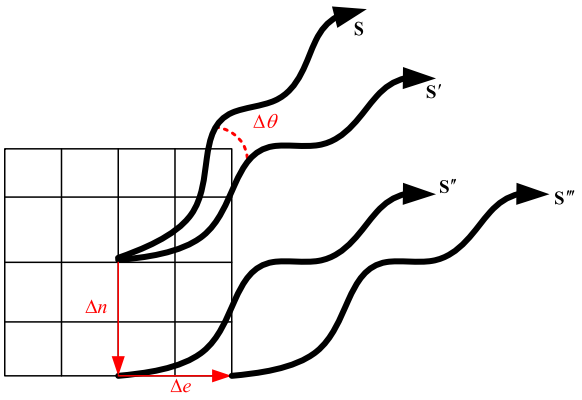

Fig. 4. Detailed process of generating a candidate reference trajectory. Δn and Δe are the translation parameters, and $\Delta\theta$ is the rotation parameter [9].

Based on the relative positions and attitudes estimated by the PDR, the observed MFP can be expressed as

$$o\text{MFP} = \left\{ \boldsymbol{r}^n_{0:k-1} \quad \left(\boldsymbol{C}^n_b\right)_{0:k-1} \quad \tilde{\boldsymbol{M}}^b_{0:k-1} \right\} \tag{17}$$

where $\tilde{M}^b$ is the output of the magnetometer and k is the number of sampling points of the observed MFP.

The problem of the MFM positioning can then be simplified as finding the conversion relationship (i.e., translation and rotation parameters) between the relative and absolute trajectories. However, the conversion relationship and the coordinates of the absolute trajectory are both unknown, so it is not possible to estimate the translation and rotation parameters using mathematical analysis methods. An alternative approach is to generate all possible reference trajectories based on the relative trajectory by traversing the possible translation and rotation parameters. Then, the conversion relationship can be determined according to the similarities between the observed and reference MFSs corresponding to the candidate reference trajectories. Fig. 4 shows the detailed process of generating a candidate reference trajectory. In this way, it is possible to obtain all possible reference trajectories by setting different translation and rotation parameters. Then, the jth point in the ith candidate trajectory and the corresponding cosine matrix can be expressed as

$$\boldsymbol{r}^{n'}_{i,j} = \boldsymbol{C}(\Delta\theta_i)\left(\boldsymbol{r}^n_j - \boldsymbol{r}^n_0\right) + \boldsymbol{r}^n_0 + \Delta\boldsymbol{r}^n_i \tag{18}$$

$$\left(\boldsymbol{C}^{n'}_b\right)_{i,j} = \left(\boldsymbol{C}^{n'}_n\right)_i \left(\boldsymbol{C}^n_b\right)_j \tag{19}$$

where

$$\boldsymbol{C}(\Delta\theta_i) = \begin{bmatrix} \cos(\Delta\theta_i) & -\sin(\Delta\theta_i) \\ \sin(\Delta\theta_i) & \cos(\Delta\theta_i) \end{bmatrix}$$

$$\left(\boldsymbol{C}^{n'}_n\right)_i = \begin{pmatrix} \boldsymbol{C}(\Delta\theta_i) & \boldsymbol{0}_{2\times 1} \\ \boldsymbol{0}_{1\times 2} & 1 \end{pmatrix}$$

where $\Delta\boldsymbol{r}^n = (\Delta n \ \Delta e)^T$ and $\Delta\theta$ are the translation and rotation parameters, respectively.

As a magnetic field map is composed of uniformly distributed reference points, the sampling points of the candidate reference trajectory cannot coincide exactly with the reference points. Therefore, here, the bilinear interpolation method is proposed to obtain a higher resolution reference MFS, as shown in Fig. 5. The corresponding reference MFS of a given point $r(n, e)$ is

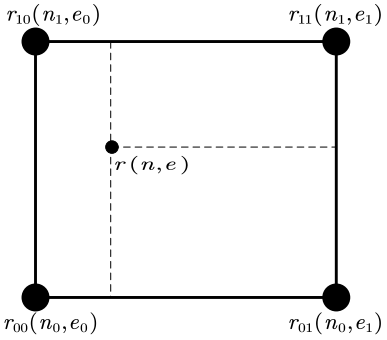

Fig. 5. Reference MFS from bilinear interpolation at $r(n, e)$ [12].

$$\boldsymbol{M}^n(r) \approx \boldsymbol{\alpha}\boldsymbol{M}^n(r_{01}) + \boldsymbol{\beta}\boldsymbol{M}^n(r_{00}) + \boldsymbol{\gamma}\boldsymbol{M}^n(r_{11}) + \boldsymbol{\chi}\boldsymbol{M}^n(r_{10}) \tag{20}$$

where

$$\boldsymbol{\alpha} = \frac{(n_1 - n)(e - e_0)}{(n_1 - n_0)(e_1 - e_0)}, \quad \boldsymbol{\beta} = \frac{(n_1 - n)(e_1 - e)}{(n_1 - n_0)(e_1 - e_0)}$$
$$\boldsymbol{\gamma} = \frac{(n - n_0)(e - e_0)}{(n_1 - n_0)(e_1 - e_0)}, \quad \boldsymbol{\chi} = \frac{(n - n_0)(e_1 - e)}{(n_1 - n_0)(e_1 - e_0)}.$$

The ith reference MFP can be expressed as

$$r\text{MFP}_i = \left(\boldsymbol{r}^{n'}_{i,0:k-1} \quad \left(\boldsymbol{C}^{n'}_b\right)_{i,0:k-1} \quad \left(\left(\boldsymbol{C}^{n'}_b\right)^T_{i,0:k-1} \boldsymbol{M}^n_{i,0:k-1} \right) \right). \tag{21}$$

As the magnetometer bias comprises a fixed value in the b-frame over short time frames, the differential MFP in the b-frame can be used to eliminate the influence of the magnetometer bias. To avoid large errors in the selected reference MFS, averaging processing is performed on the observed and reference MFPs in the proposed method. The DTW algorithm is then used to calculate the similarity between the observed and reference MFPs. The DTW compresses or stretches the reference axes of the two sequences to be matched such that two sequences with different lengths will have better matching results [29]. This will help to solve the problem that the empirical step model cannot accurately estimate the step lengths of different users.

C. MFM/PDR Integrated Positioning

In the proposed method, the MFM results are used to control the position drift of the INS-based PDR. This helps to improve the estimation accuracy of the relative trajectory (e.g., the scale of step length) and provides a more accurate location search area than the pure PDR for the magnetic matching (MM) method. The position observation equation in the n-frame is given as follows:

$$\delta\boldsymbol{z}_r = \hat{\boldsymbol{r}}^n - \tilde{\boldsymbol{r}}^n = \delta\boldsymbol{r}^n + \boldsymbol{\sigma}_r \tag{22}$$

where $\hat{\boldsymbol{r}}^n$ is the estimated position from the INS-based PDR, $\tilde{\boldsymbol{r}}^n$ is the result of the MFM, and $\boldsymbol{\sigma}_r$ is the noise of the position measurement. The gradient and residual error corresponding

to the MFP can be used to determine the noise of the MFM results as follows [41]:

$$\boldsymbol{\sigma}_r = \left(\boldsymbol{H}^T \boldsymbol{H}\right)^T \sigma_0 \tag{23}$$

$$\boldsymbol{\sigma}_0 = \sqrt{\frac{\sum_{j=0}^{k-1} \left\| \tilde{\boldsymbol{M}}_j^n - \boldsymbol{M}_j^n \right\|}{k}} \tag{24}$$

$$\boldsymbol{H} = \begin{bmatrix} \boldsymbol{H}_0 & \cdots & \boldsymbol{H}_{k-1} \end{bmatrix}^T \tag{25}$$

$$\boldsymbol{H}_j = \left(\frac{\partial \boldsymbol{M}^n(r_j)}{\partial n} \quad \frac{\partial \boldsymbol{M}^n(\boldsymbol{r}_j)}{\partial e} \right) \frac{\partial \boldsymbol{r}_j(\boldsymbol{\xi})}{\partial \boldsymbol{\xi}} \tag{26}$$

where $\tilde{\boldsymbol{M}}^n$ is the output of the magnetometer in the n-frame, $\boldsymbol{M}^n$ is the reference magnetic field vector in the n-frame from the magnetic field map, and $(\partial \boldsymbol{M}^n(r_j)/\partial n)$ and $(\partial \boldsymbol{M}^n(r_j)/\partial e)$ are the magnetic field gradients

$$\frac{\partial \boldsymbol{M}^n(r_j)}{\partial n} \approx \frac{e - e_0}{(n_1 - n_0)(e_1 - e_0)} (\boldsymbol{M}(r_{11}) - \boldsymbol{M}(r_{01})) + \frac{e_1 - e}{(n_1 - n_0)(e_1 - e_0)} (\boldsymbol{M}(r_{10}) - \boldsymbol{M}(r_{00})) \tag{27}$$

$$\frac{\partial \boldsymbol{M}^n(r_j)}{\partial e} \approx \frac{n - n_0}{(n_1 - n_0)(e_1 - e_0)} (\boldsymbol{M}(r_{11}) - \boldsymbol{M}(r_{10})) + \frac{n_1 - n}{(n_1 - n_0)(e_1 - e_0)} (\boldsymbol{M}(r_{01}) - \boldsymbol{M}(r_{00})). \tag{28}$$

$(\partial \boldsymbol{r}_j(\xi)/\partial \xi)$ is the partial derivative of the absolute position with respect to the translation and rotation parameters

$$\frac{\partial \boldsymbol{r}_j(\xi)}{\partial \xi} = \begin{bmatrix} 1 & 0 & -\sin(\Delta\theta)\Delta n_{j-0} - \cos(\Delta\theta)\Delta e_{j-0} \\ 0 & 1 & \cos(\Delta\theta)\Delta n_{j-0} - \sin(\Delta\theta)\Delta e_{j-0} \end{bmatrix} \tag{29}$$

where

$$\boldsymbol{\xi} = [\Delta n, \Delta e, \Delta\theta]^T$$

$$\boldsymbol{r}(\boldsymbol{\xi}) = \begin{bmatrix} \cos(\Delta\theta) & -\sin(\Delta\theta) \\ \sin(\Delta\theta) & \cos(\Delta\theta) \end{bmatrix} \begin{bmatrix} \Delta n_{j-0} \\ \Delta e_{j-0} \end{bmatrix} + \begin{bmatrix} n_0 + \Delta n \\ e_0 + \Delta e \end{bmatrix}.$$

$\Delta n_{j-0} = n_j - n_0$ is the position increment coming from INS-based PDR, where n_0 is the first point of an observed MFP.

VI. Test Results and Analysis

A. Test Description

Field tests were conducted on the second floor of the Shilintong International Geospatial Information Science Research Center of Wuhan University. The test area was a typical indoor office environment. Fig. 6 shows the real environment of the test area. As this building was not in full use at the time of the experiment, many rooms were not equipped with any office facilities. Therefore, the magnetic field interference in the corridor area was more obvious than that in the empty room. The size of the test area was 94 × 22 m, about 2000 m^2. Fig. 7 shows the indoor structure; the red box shows the test area.

Nine Android smartphones were used, including a Huawei Mate 20, Xiaomi 8, Oneplus 6T, Huawei P10, Samsung Galaxy S6, Samsung Galaxy S10, Honor V10, Google Pixel 2, and Google Pixel 3. The data rates were set at 50 Hz for the gyroscopes, accelerometers, and magnetometers. The

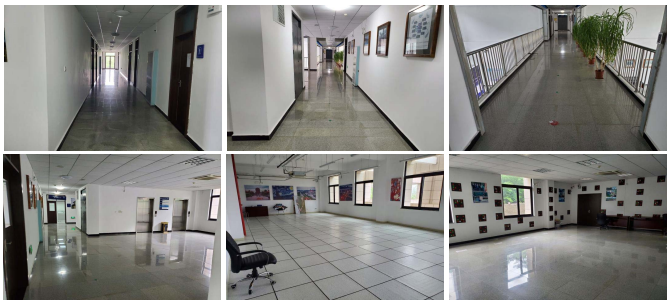

Fig. 6. Test environment.

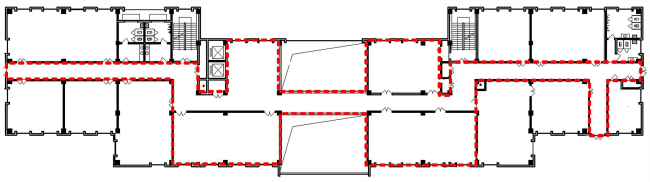

Fig. 7. Floor plan. The area covered by the red dotted line represents the effective test area.

foot-mounted IMU of the P-POS in each case was an Invensense ICM-20602, and the bias instabilities of the gyroscopes and accelerometers were set as 60°/s and 0.2 mg, respectively. The data rate of each foot-mounted IMU was set at 200 Hz. The system times of the smartphones and foot-mounted IMUs were aligned via Bluetooth communication. All sensor data were logged into files for postprocessing.

In the magnetic field map generation and real-time positioning stages, the P-POS consisted of a foot-mounted IMU and a smartphone; this was used to provide a high-precision position and attitude for the smartphone. Due to the limited space, this article will not evaluate the pose estimation accuracy of P-POS in detail. For the specific evaluation methods and the estimation accuracy of the P-POS, please refer to [35].

B. Magnetic Field Map

Three smartphones (Pixel 2, Pixel 3, and Xiaomi 8) were employed to collect the magnetic field data of the test area, and the average time spent was 13.7 min. The test area was approximately 2000 m^2; therefore, the average data collection efficiency of the magnetic field map was approximately 145 m^2/min. If the test area was a 50 × 20 open indoor area (i.e., in extreme cases), the tester followed the *S*-shaped walking rule at normal velocity (i.e., walk at a speed of 1.2 m/s and the distance interval between adjacent trajectories was 2 m), and the data collection efficiency still reached 122 m^2/min.

Fig. 8 shows the trajectories of data collection. The blue, red, and yellow lines represent the trajectories of data collection in the three regions, and the red dots are the reference points. The proposed method allows users to walk trajectories of different shapes and requires 19 reference points in total. Using the traditional method, 53 straight lines were required to achieve the same density of data acquisition, for a total of 106 reference points. The demand for control

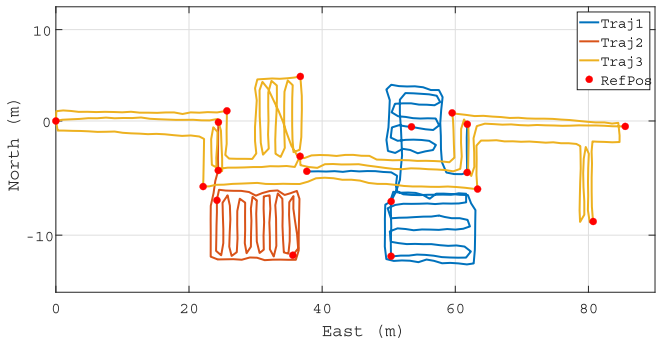

Fig. 8. Trajectories of data collection.

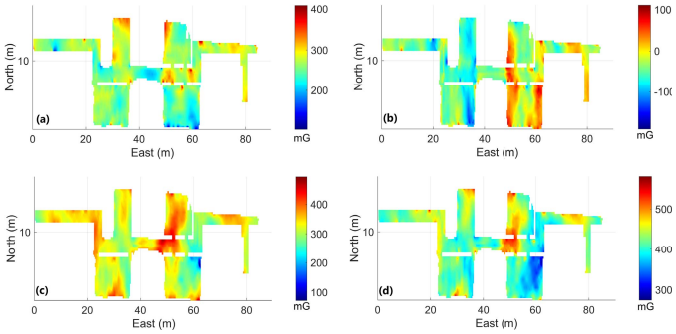

Fig. 9. Magnetic field map using Google Pixel 2. (a) North component. (b) East component. (c) Vertical component. (d) Magnitude.

points was reduced by 82%. Fig. 9 shows the magnetic field map constructed by using Google Pixel 2. Although magnetic field features were collected using different phone poses, the MFS of adjacent geographic locations shows gentle transitions, which is consistent with the objective physical phenomena. We can see that the magnetometer bias was well compensated and corrected, and P-POS could provide high-precision pose estimation results.

To further verify the effectiveness of the proposed method, the magnetic field maps were constructed multiple times using different smartphones and the differences in MFS at the same position were used to define the accuracy of the magnetic field map generation method. Fig. 10 shows the differences between the magnetic field maps constructed by using Google Pixel 2 and Mi 8. These differences in most regions were around zero, and the differences in some areas reached approximately 100 mG. This is because the accuracy of P-POS is limited (approximately decimeter level). Moreover, the MFS decay with the 3rd power of the spatial distance, small position, and attitude errors caused obvious MFS deviations near magnetic field interference sources.

Fig. 11 shows the cumulative distribution function of the differences between the magnetic field maps constructed by using different smartphones. Table I summarizes the root-mean-square (rms) values, alongside 68% and 95% of the differences in the magnetic field maps constructed by using different smartphones. The differences in the magnetic field maps between any two smartphones were <20 mG (rms); 95% of these differences were <40 mG. The differences in the three directions are not significantly larger than the

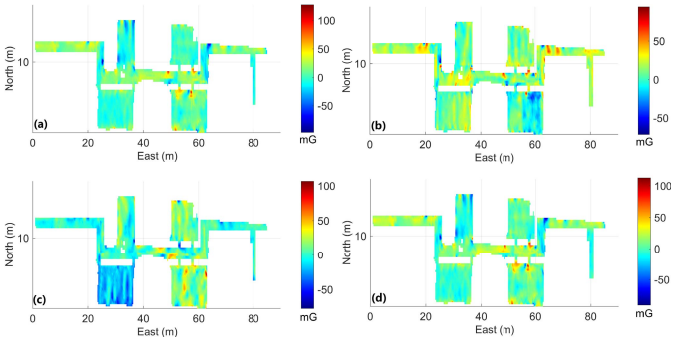

Fig. 10. Differences between the magnetic field maps using Mi 8 and Google Pixel 2. (a) North component. (b) East component. (c) Vertical component. (d) Magnitude.

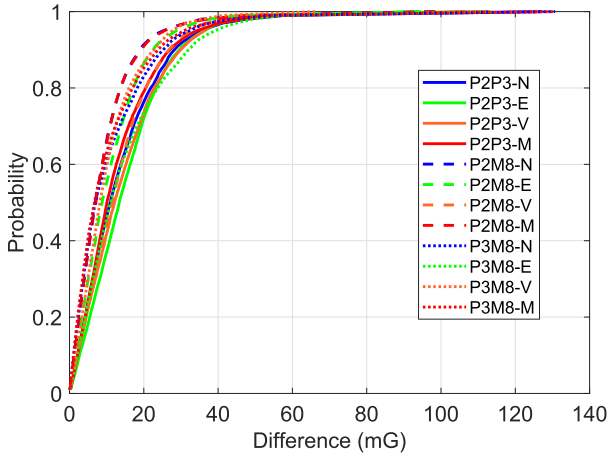

Fig. 11. Cumulative distribution function of differences between magnetic field maps constructed by different smartphones.

TABLE I

RMS AND 68% AND 95% OF THE DIFFERENCES IN THE MAGNETIC FIELD MAPS CONSTRUCTED USING DIFFERENT SMARTPHONES

	Pixel2-Pixel3 (mG)			Pixel2-Mi8(mG)			Pixel3-Mi8 (mG)		
	RMS	68%	95%	RMS	68%	95%	RMS	68%	95%
North	18.4	16.2	35.6	13.0	10.1	25.2	16.0	12.1	32.3
East	19.1	18.3	36.3	14.7	13.1	28.7	19.4	16.7	39.1
Vertical	18.4	17.6	36.2	17.0	15.8	32.6	13.6	11.6	27.7
Magnitude	17.5	14.8	34.2	13.0	10.2	25.6	15.4	11.2	30.8

magnitude, which indirectly indicates that the attitude provided by P-POS has high enough accuracy, and the magnetometer bias is well estimated and compensated. The noise levels of the built-in magnetometers in most smartphones are approximately 10–20 mG, so the errors caused by P-POS and the map generation algorithms were relatively very small. Therefore, the magnetic field map generation method proposed in this article was shown to be highly efficient and precise.

Table II summarizes currently used magnetic field mapping methods that have been presented in other papers, including point-by-point [17], [42], [43], WS [18], and SLAM [24]. The crowdsourcing methods are not listed in the table because their main advantage is low labor cost. Moreover, crowdsourcing methods are very dependent on the real movement trajectories

TABLE II
MAPPING PERFORMANCE COMPARISON WITH STATE-OF-THE-ART METHODS

Methods	Accuracy (m)	Efficiency (m^2/h)	Cost	Complexity	Calibration
[42]	0.06	260	high	high	Yes
[17]	0.1	300	middle	high	Yes
[20]	0.3	600	high	low	Yes
[43]	0.3	600	middle	high	Yes
[18]	0.3	1800	low	high	Yes
Proposed	0.1	7200	middle	middle	No

Accuracy is the coordinate accuracy of the location label; Efficiency is the area of data collected per hour; Cost is the equipment cost; Complexity is the percentage of time that testers need to intervene; Calibration is the need to actively calibrate the magnetometer bias.

of mass users and have very large random characteristics, so their efficiency and accuracy cannot be quantitatively described. According to the comparison, we find that the proposed method achieves the highest measurement efficiency and is the only method that does not require active calibration of the magnetometer bias. The accuracy of the proposed method is slightly worse than that of the method [42], but it is sufficient for the needs of pedestrian localization. The hardware cost of the proposed method includes a foot-mounted IMU and a smartphone, the cost of the foot-mounted IMU does not exceed U.S. $10, and the cost of the smartphone can be ignored to some extent due to the high ownership rate. Therefore, compared with method in [18], the cost increase of the proposed method is very limited. As the step of actively labeling the position cannot be omitted, the proposed method has a higher complexity than that shown by the method of [20]. However, this does not affect the conclusion that the proposed method has a better performance than existing methods under the comprehensive metrics of accuracy, efficiency, cost, complexity, and calibration.

C. Positioning Performance

This section evaluates the positioning accuracy of four positioning schemes: 1) PDR, as described in section V-A; 2) MFM, as described in Section V-B, in which the relative trajectory generated by PDR is used to generate the MFP; 3) MFM/PDR, in which PDR is used to generate the MFP, while the output of the MM is used to control the position error of the PDR (the noise of the MM output is given a fixed value); and 4) adaptive MFM/PDR (AMFM/PDR), which is similar to 3), but differs in that the noise of the MM output is automatically given by the method described in Section V-C.

In total, 16 tests were conducted using eight different smartphones (Mate 20, Mi 8, Oneplus 6T, P10, S6, S10, V10, and Pixel 2) based on the magnetic field map of Google Pixel 2. As an MFP does not have a unique identification, the initial phase of MFM positioning usually relies on other positioning methods to provide a rough location (such as a position error < 20 m) to assist in determining the magnetic field fingerprint map [9]. Here, the initial position was manually given; Wi-Fi/Bluetooth was used to provide a rough position in the actual application scenarios.

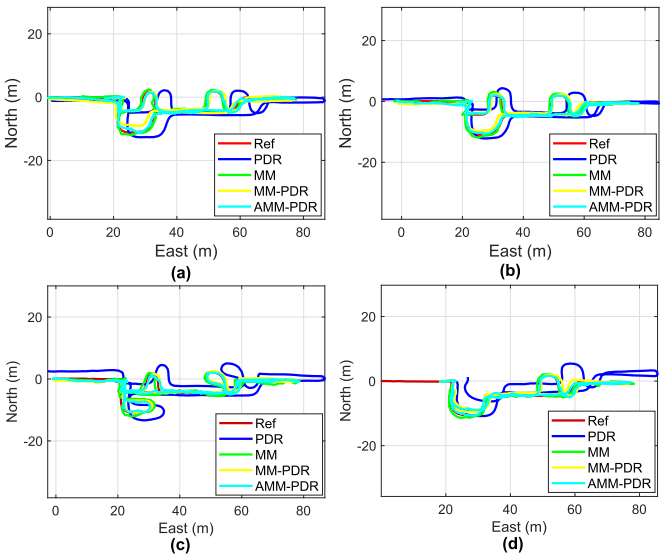

Fig. 12. Trajectories of reference for PDR, MFM, MFM/PDR, and AMFM/PDR. (a) V10-1. (b) S10-1. (c) Mi8-1. (d) Pixel2-1.

To simulate the walking habits of ordinary users, the testers walked in straight trajectories in the corridor area and irregularly shaped curves in the room area. The trajectories of the four tests of the four smartphones are shown in Fig. 12; the other 12 test trajectories were similar. The trajectories generated by the PDR had different scales and deformation errors in the different tests. The scale error caused by the step-length estimation model was greater than the trajectory shape deformation caused by the heading error. This was because the heading drift error could be well suppressed by the attitude filtering method, but the step-length estimation model could not adapt to different users, due to factors such as the user's height, weight, and walking style. Nevertheless, MFM, MFM/PDR, and AMFM/PDR all achieved stable positioning performance. Thus, it was shown that the relative trajectory with error generated by the PDR could effectively assist the MFM positioning.

Fig. 13 shows the cumulative density function of the position errors of the four positioning schemes across 16 tests; "Mate20-1" is the first test of the Huawei Mate 20. Table III lists the RMS and 68% and 95% of the positioning error of the four positioning schemes across 16 tests. The mean position errors of PDR, MFM, MFM/PDR, and AMFM/PDR were 6.378, 1.148, 1.085, and 0.812 m, respectively. Compared with MFM, MFM/PDR showed no obvious positioning performance improvement; in fact, it even performed worse in some tests (such as S10-2, OnePlus 6T-2, and V10-2). This may have occurred because unreasonable MFM position noise may have destroyed the stability of the filter and reduced its estimation performance, thus resulting in greater positioning errors. Compared with MFM and MFM/PDR, AMFM/PDR achieved smaller positioning errors, its positioning performance improved by 25% and 29%, respectively. AMFM/PDR uses reasonable noise for the MFM position; it achieved the best estimate of data fusion. This confirms the validity of the magnetic field positioning error estimation method proposed in this article.

TABLE III

RMS, 68%, AND 95% OF THE POSITION ERRORS OF PDR, MFM, MFM/PDR, AND AMFM/PDR IN 16 TESTS

Test	PDR (m)			MFM (m)			MFM/PDR (m)			AMFM/PDR (m)		
	RMS	68%	95%	RMS	68%	95%	RMS	68%	95%	RMS	68%	95%
Mate20-1	7.334	8.160	10.251	1.367	1.301	2.219	1.143	1.150	1.841	0.922	0.969	1.677
Mate20-2	6.440	7.326	9.361	1.371	1.268	2.714	1.084	1.116	1.959	0.933	0.833	1.909
Mi8-1	5.365	5.886	8.730	1.504	1.504	2.516	0.828	0.884	1.427	0.835	0.869	1.434
Mi8-2	6.670	7.221	9.694	1.258	1.259	2.184	0.771	0.779	1.415	0.677	0.697	1.266
OnePlus6T-1	5.578	6.597	9.310	1.066	1.117	1.729	1.088	1.176	1.880	0.749	0.839	1.388
OnePlus6T-2	6.692	7.249	9.796	1.103	1.231	1.713	1.307	1.263	2.514	1.035	0.941	2.223
P10-1	5.690	6.453	8.876	1.040	1.005	1.560	1.054	1.052	1.848	0.917	0.792	1.841
P10-2	6.114	7.107	9.226	1.373	1.355	2.339	1.216	1.125	2.385	0.944	0.883	1.828
S10-1	4.506	4.966	6.907	0.957	1.016	1.478	0.843	0.881	1.422	0.634	0.672	1.078
S10-2	6.932	7.900	10.117	0.951	1.111	1.369	1.469	1.448	2.566	0.926	1.004	1.542
S6-1	6.603	7.362	8.966	1.046	1.093	1.649	1.151	1.261	1.730	0.776	0.834	1.290
S6-2	8.439	9.090	11.758	0.937	0.989	1.487	1.028	1.115	1.618	0.706	0.737	1.232
V10-1	6.463	7.223	9.628	1.072	1.201	1.659	1.187	1.282	2.079	0.715	0.745	1.285
V10-2	6.095	6.812	8.783	1.062	1.088	1.686	1.377	1.490	2.455	0.880	0.975	1.532
Pixel2-1	6.958	7.979	10.714	0.938	0.994	1.509	0.912	0.971	1.505	0.641	0.608	1.252
Pixel2-1	6.176	7.113	8.701	1.326	1.228	2.380	0.917	0.879	1.667	0.709	0.645	1.321
Mean	6.378	7.152	9.426	1.148	1.172	1.886	1.085	1.117	1.894	0.812	0.815	1.506

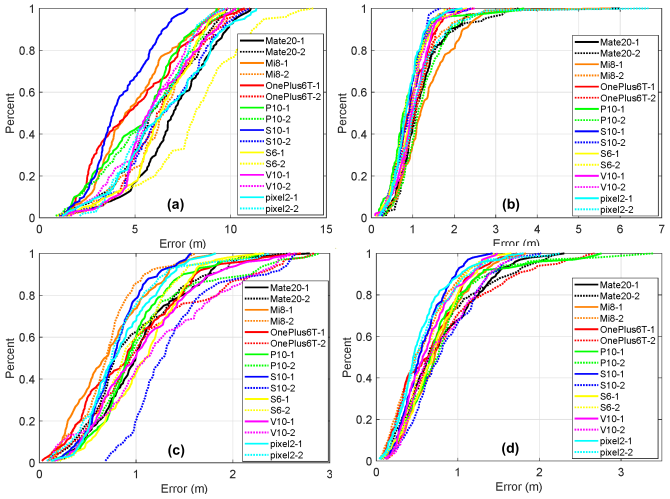

Fig. 13. Cumulative density function of position errors for four positioning schemes over 16 tests. (a) PDR. (b) MFM. (c) MFM/PDR. (d) AMFM/PDR.

TABLE IV

POSITIONING PERFORMANCE COMPARISON WITH THE STATE-OF-THE-ART SCHEMES

Scheme	Techniques	Scenarios	Size (m^2)	Accuracy (m)
[49]	DTW, PF	Shopping mall	9510	∼5.0
[11]	DTW	Corridor	4000	∼5.0
[29]	DTW	Corridor	/	3.5
[30]	DTW	Corridor	/	∼2.0
[44]	PF	Corridor, Room, Hall,	/	∼2.0
[45]	PF	Corridor	45	1.7
[46]	PF	Corridor	120	1.0
[47]	PF	Corridor	700	0.8
[48]	PF	Book shelf	350	0.8
Proposed	DTW	Corridor, Room, Hall	2000	0.8
[28]	PF	Room	450	0.4

DTW∼Dynamic Time Warp, PF∼Particle Filter, UPL∼Underground Parking Lot.

The positioning errors of AMFM/PDR in the 16 tests were distributed between 0.64 and 1.04 m (rms); the floating range was approximately 0.4 m. Compared with the length of a pedestrian step (approximately 0.65 m), the fluctuation range of the positioning error was small. There were no obvious differences in positioning performance across the 16 tests when using different terminals. This was because the differences in the users' walking styles were weakened by using the PDR to estimate their walking trajectories in real time; at the same time, the differences between different magnetometers were also weakened by using the differential MFP under the *b*-frame system to eliminate each magnetometer's zero bias. In addition, the average positioning error of the 16 tests was 0.81 m (rms), showing that the proposed method could obtain submeter-level positioning in office buildings.

Table IV summarizes currently used algorithms that have been presented in other papers; those algorithms used magnetic field fingerprint-based matching methods and inertial sensors. Although the test scenarios were different, the test results can roughly reflect the positioning performances between different algorithms. The proposed method achieves a higher positioning performance than all of the DTW-based studies [11], [29], [30]. The main improvements of the proposed method include: 1) the relative trajectory generated by PDR can truly reflect the user's walking trajectory and 2) the differential MFP improves the position discrimination of the MFS and weakens the influences of errors arising from magnetometer bias and the inaccurate local magnetic field maps. The proposed method also achieves a positioning performance similar to those of PF-based studies [44], [45], [46], [47], [48] but is worse than the latest method [28]. The possible reasons for [28] to achieve such impressive positioning accuracy include improvements in the probabilistic model, large particle numbers (e.g., 10 000), smaller localization regions, and higher position discrimination of magnetic field features within the region. However,

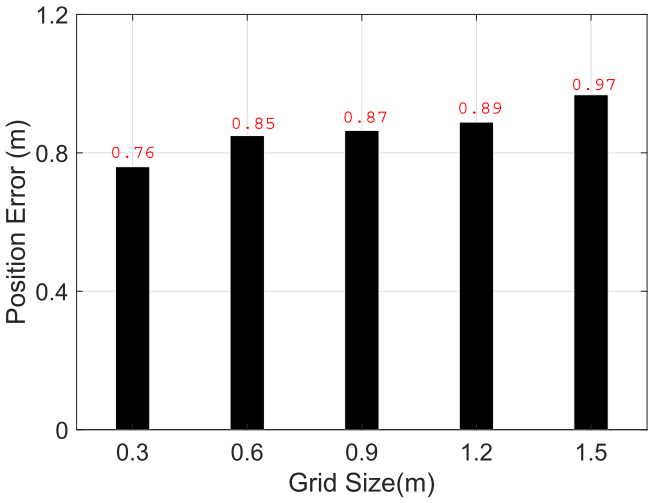

Fig. 14. Mean rms of the position errors of MFM using different grid sizes in 16 tests.

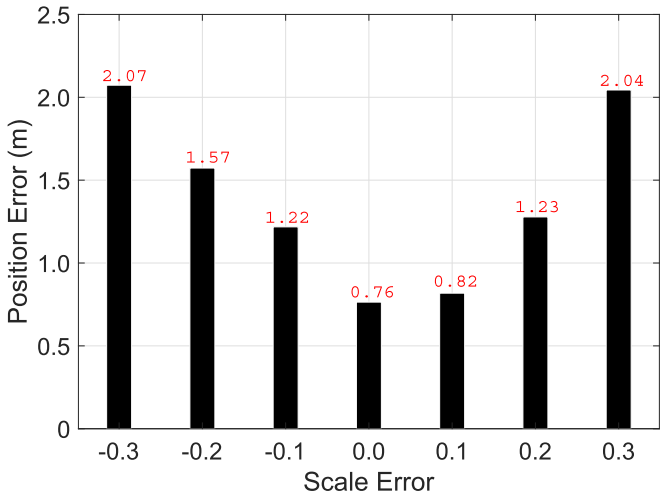

Fig. 15. Mean rms of MFM position errors for different step-length scale errors across 16 tests.

the accuracy improvement of several decimeters is not obvious, especially for the mass users' meter-level positioning accuracy requirements. Therefore, we can still reach the conclusion that the proposed method effectively reduces the computational load while achieving a positioning performance close to that of the PF-based methods.

D. Parameters Setting for MFM

This section mainly analyzes the impacts of different parameter configurations on the positioning performance of the MFM. These parameters include the resolution of the magnetic field map, length, deformation error, and scale error of the MFP. The length of the MFP has been discussed in detail in many papers [50]. The length of the MFP used in this study was approximately 13 m. The deformation error of the MFP mainly refers to the heading angle drift error of the PDR, which is not described in detail here. The attitude heading reference systems described in many studies can slow the heading angle drift to less than 10° per 100 m [51]; the deformation error can be reduced to less than $13*\tan(13/100*10) \approx 0.29$ m. Compared with the length of the MFP, the deformation error in the proposed model was very small.

The resolution of a magnetic field map determines the position resolution of the corresponding MFM. Based on ensuring the positioning performance, a reasonable set of magnetic field map resolution can effectively reduce the system cost and storage space required for the magnetic field map. Fig. 14 shows the mean rms of the position errors of MFM at different grid sizes across the 16 tests. As the grid size of the magnetic field map increased from 0.3 to 1.5 m, the average rms of the position errors of the 16 tests rose from 0.76 to 0.97 m, while the positioning performance dropped by approximately 27.6%. To achieve the highest positioning performance, the resolution of a magnetic field map should theoretically be set to be as small as possible. However, the accuracy of the reference point coordinates in a magnetic field map is positively correlated with the cost of data collection. In practical applications, it is usually necessary to consider both the positioning performance and cost to economize the system while meeting the positioning requirements. In this study, P-POS provided decimeter-level positions at a very low cost, so the resolution of the magnetic field map was set as 0.3 m.

Empirical step-length estimation models cannot adapt to different users, so the proportional error of the MFP is the main error source of the MFM in the real-time positioning stage. Here, simulation methods were used to evaluate the influence of the scale error of the step-length estimation model on the MFM positioning performance. First, P-POS was used to obtain accurate scale parameters for the step-length model. Then, a model with a known scale error was obtained by adding different scale errors to this accurate model. Finally, this step-length estimation model with the error was used for MFM positioning. Fig. 15 shows the mean rms of the MFM position errors under different scale errors for the estimated step length, across 16 tests. The position error of the MFM gradually increased with increasing proportional error. Nevertheless, a proportional error of <0.3 could still effectively assist the MFM and positioning. The proportional error of the empirical step-length estimations model is usually better than 0.1, so it is reasonable to use an empirical step-length estimation model to ensure that the MFM works normally [10]. More importantly, MFM/PDR can estimate the proportional error of the empirical step-length estimation model in real time, which allows for the model to adapt to different users.

VII. Conclusion and Future Work

This study focused on providing an efficient and robust magnetic field positioning solution. By taking advantage of the relative positioning and attitude estimation abilities of consumer-grade IMUs, a method was developed for efficiently constructing a stable magnetic field map with real-time positioning. During the magnetic field map generation stage, this method used P-POS, comprising a foot-mounted IMU and a built-in smartphone IMU, to provide decimeter-level positioning and degree-level attitude (including roll, pitch,

and heading) for a smartphone. The test results for three different smartphones showed that the magnetic data collection efficiency of the proposed method reached 37 m^2/min and that the differences in the magnetic field maps constructed by the three smartphones were less than 20 mG (rms).

In the real-time positioning stage, the proposed method uses the position and attitude provided by PDR for the differential MFP in the *b*-frame; this can eliminate the impact of magnetometer bias. A new position noise estimation method was also proposed based on the magnetic field gradient; it can effectively improve the accuracy of the MFM/PDR integrated positioning algorithm. The results of 16 field tests conducted using eight smartphones delivered positioning errors distributed between 0.64 and 1.04 m (rms), reaching an average positioning performance of 0.81 m (rms). These experimental results verified that the MFM positioning method designed in this study is less affected by magnetometer bias and can provide consistent positioning performance across different smartphone terminals.

As the smartphone-based indoor MFM positioning scheme proposed in this study is highly dependent on the stability of PDR, future studies should focus on automatically monitoring the integrity of PDR and applying the proposed scheme to a variety of typical smartphone modes (such as texting, calling, and swinging). In addition, whether the differential MFP can effectively eliminate the absolute difference of the magnetic field at different heights described in the work of [42] needs more sufficient testing and verification, especially in the scene of height changes caused by the same person holding the phone. Furthermore, a method for generating magnetic field maps based on crowd-sourced data should be explored to further reduce the cost of generating magnetic field maps.

REFERENCES

[1] J. Wahlström, I. Skog, and P. Händel, "Smartphone-based vehicle telematics: A ten-year anniversary," *IEEE Trans. Intell. Transp. Syst.*, vol. 18, no. 10, pp. 2802–2825, Oct. 2017.

[2] R. Chen and L. Chen, "Smartphone-based indoor positioning technologies," in *Urban Informatics*. Singapore: Springer, 2021, pp. 467–490.

[3] N. El-Sheimy and Y. Li, "Indoor navigation: State of the art and future trends," *Satell. Navigat.*, vol. 2, no. 7, pp. 1–23, 2021.

[4] X. Cao, Y. Zhuang, X. Yang, X. Sun, and X. Wang, "A universal Wi-Fi fingerprint localization method based on machine learning and sample differences," *Satell. Navigat.*, vol. 2, no. 1, pp. 1–15, Dec. 2021.

[5] J. Chen et al., "A data-driven inertial navigation/bluetooth fusion algorithm for indoor localization," *IEEE Sensors J.*, vol. 22, no. 6, pp. 5288–5301, Mar. 2021.

[6] A. Bekkali, H. Sanson, and M. Matsumoto, "RFID indoor positioning based on probabilistic RFID map and Kalman filtering," in *Proc. 3rd IEEE Int. Conf. Wireless Mobile Comput., Netw. Commun. (WiMob)*, Oct. 2007, p. 21.

[7] J. Liu, K. Gao, W. Guo, J. Cui, and C. Guo, "Role, path, and vision of "5G+BDS/GNSS," *Satell. Navigat.*, vol. 1, no. 1, p. 23, Dec. 2020.

[8] B. Van Herbruggen et al., "Wi-PoS: A low-cost, open source ultra-wideband (UWB) hardware platform with long range sub-GHz backbone," *Sensors*, vol. 19, no. 7, p. 1548, 2019.

[9] J. Kuang, T. Li, and X. Niu, "Magnetometer bias insensitive magnetic field matching based on pedestrian dead reckoning for smartphone indoor positioning," *IEEE Sensors J.*, vol. 22, no. 6, pp. 4790–4799, Mar. 2022.

[10] J. Kuang, X. Niu, and X. Chen, "Robust pedestrian dead reckoning based on MEMS-IMU for smartphones," *Sensors*, vol. 18, no. 5, p. 1391, 2018.

[11] Y. Shu, C. Bo, G. Shen, C. Zhao, L. Li, and F. Zhao, "Magicol: Indoor localization using pervasive magnetic field and opportunistic WiFi sensing," *IEEE J. Sel. Areas Commun.*, vol. 33, no. 7, pp. 1443–1457, May 2015.

[12] J. Kuang, X. Niu, P. Zhang, and X. Chen, "Indoor positioning based on pedestrian dead reckoning and magnetic field matching for smartphones," *Sensors*, vol. 18, no. 12, p. 4142, Nov. 2018.

[13] D. Liu, S. Guo, Y. Yang, Y. Shi, and M. Chen, "Geomagnetism-based indoor navigation by offloading strategy in NB-IoT," *IEEE Internet Things J.*, vol. 6, no. 3, pp. 4074–4084, Jun. 2018.

[14] B. Wang, J. Zhu, Z. Deng, and M. Fu, "A characteristic parameter matching algorithm for gravity-aided navigation of underwater vehicles," *IEEE Trans. Ind. Electron*, vol. 66, no. 2, pp. 1203–1212, Feb. 2018.

[15] C. E. Galván-Tejada, J. P. García-Vázquez, and R. F. Brena, "Magnetic field feature extraction and selection for indoor location estimation," *Sensors*, vol. 14, no. 6, pp. 11001–11015, 2014.

[16] M. Perttunen. (2021). *IndoorAtlas Support*. [Online]. Available: https://indooratlas.freshdesk.com/support/home

[17] I. Ashraf, S. Din, M. U. Ali, S. Hur, Y. B. Zikria, and Y. Park, "MagWi: Benchmark dataset for long term magnetic field and Wi-Fi data involving heterogeneous smartphones, multiple orientations, spatial diversity and multi-floor buildings," *IEEE Access*, vol. 9, pp. 77976–77996, 2021.

[18] G. Liu, B. Yu, L. Huang, L. Shi, X. Gao, and L. He, "Human-interactive mapping method for indoor magnetic based on low-cost MARG sensors," *IEEE Trans. Instrum. Meas.*, vol. 70, pp. 1–10, 2021.

[19] E. Le Grand and S. Thrun, "3-axis magnetic field mapping and fusion for indoor localization," in *Proc. IEEE Int. Conf. Multisensor Fusion Integr. Intell. Syst. (MFI)*, Sep. 2012, pp. 358–364.

[20] P. Robertson et al., "Simultaneous localization and mapping for pedestrians using distortions of the local magnetic field intensity in large indoor environments," in *Proc. Int. Conf. Indoor Positioning Indoor Navigat.*, 2013, pp. 1–10.

[21] B. Zhou et al., "Crowdsourcing-based indoor mapping using smartphones: A survey," *ISPRS J. Photogramm. Remote Sens.*, vol. 177, pp. 131–146, Jul. 2021.

[22] W. Zhao, S. Han, R. Q. Hu, W. Meng, and Z. Jia, "Crowdsourcing and multisource fusion-based fingerprint sensing in smartphone localization," *IEEE Sensors J.*, vol. 18, no. 8, pp. 3236–3247, Aug. 2018.

[23] A. Ayanoglu, D. M. Schneider, and B. Eitel, "Crowdsourcing-based magnetic map generation for indoor localization," in *Proc. Int. Conf. Indoor Positioning Indoor Navigat. (IPIN)*, Sep. 2018, pp. 1–8.

[24] M. Kwak, C. Hamm, S. Park, and T. T. Kwon, "Magnetic field based indoor localization system: A crowdsourcing approach," in *Proc. Int. Conf. Indoor Positioning Indoor Navigat. (IPIN)*, Sep. 2019, pp. 1–8.

[25] W. Storms, J. Shockley, and J. Raquet, "Magnetic field navigation in an indoor environment," in *Proc. Ubiquitous Positioning Indoor Navigat. Location Based Service*, 2010, pp. 1–10.

[26] *Ambient Magnetic Field-Based Indoor Location Technology: Bringing the Compass to the Next Level*, IndoorAtlas Ltd, Finland, 2012.

[27] B. Kim and S.-H. Kong, "A novel indoor positioning technique using magnetic fingerprint difference," *IEEE Trans. Instrum. Meas.*, vol. 65, no. 9, pp. 2035–2045, Sep. 2016.

[28] L.-F. Shi, M.-X. Yu, and W. Yin, "PDR/geomagnetic fusion localization method based on AOFA-improved particle filter," *IEEE Trans. Instrum. Meas.*, vol. 71, pp. 1–9, 2021.

[29] K. P. Subbu, B. Gozick, and R. Dantu, "LocateMe: Magnetic-fields-based indoor localization using smartphones," *ACM Trans. Intell. Syst. Technol.*, vol. 4, no. 4, pp. 1–27, 2013.

[30] Y. Shu, K. G. Shin, T. He, and J. Chen, "Last-mile navigation using smartphones," in *Proc. 21st Annu. Int. Conf. Mobile Comput. Netw.*, Sep. 2015, pp. 512–524.

[31] H. Wu, S. He, and S.-H. G. Chan, "Efficient sequence matching and path construction for geomagnetic indoor localization," in *Proc. Int. Conf. Embedded Wireless Syst. Netw.*, 2017, pp. 156–167.

[32] M. Sun, Y. Wang, S. Xu, H. Yang, and K. Zhang, "Indoor geomagnetic positioning using the enhanced genetic algorithm-based extreme learning machine," *IEEE Trans. Instrum. Meas.*, vol. 70, pp. 1–11, 2021.

[33] M. Zhang, J. Jia, J. Chen, L. Yang, L. Guo, and X. Wang, "Real-time indoor localization using smartphone magnetic with LSTM networks," *Neural Comput. Appl.*, vol. 33, no. 16, pp. 10093–10110, 2021.

[34] Y. Wu, D. Zou, P. Liu, and W. Yu, "Dynamic magnetometer calibration and alignment to inertial sensors by Kalman filtering," *IEEE Trans. Control Syst. Technol.*, vol. 26, no. 2, pp. 716–723, Mar. 2017.

[35] X. Niu, T. Liu, J. Kuang, and Y. Li, "A novel position and orientation system for pedestrian indoor mobile mapping system," *IEEE Sensors J.*, vol. 21, no. 2, pp. 2104–2114, Jan. 2020.

[36] J. Liu, R. Chen, L. Pei, R. Guinness, and H. Kuusniemi, "A hybrid smartphone indoor positioning solution for mobile lbs," *Sensors*, vol. 12, no. 12, pp. 17208–17233, 2012.

[37] Y. Wang, J. Kuang, Y. Li, and X. Niu, "Magnetic field-enhanced learning-based inertial odometry for indoor pedestrian," *IEEE Trans. Instrum. Meas.*, vol. 71, pp. 1–13, 2022.
[38] E. Thébault et al., "International geomagnetic reference field: The 12th generation," *Earth, Planets Space*, vol. 67, no. 1, pp. 1–19, 2015.
[39] S. Hensel, M. B. Marinov, T. Schwilk, and D. Nikolov, "Application of Gaussian process estimation for magnetic field mapping," in *Proc. Int. Conf. Future Access Enablers Ubiquitous Intell. Infrastruct.* Cham, Switzerland: Springer, 2021, pp. 284–298.
[40] E. Foxlin, "Pedestrian tracking with shoe-mounted inertial sensors," *IEEE Comput. Graph. Appl.*, vol. 25, no. 6, pp. 38–46, Nov. 2005.
[41] Y. Yang and W. Gao, "An optimal adaptive Kalman filter," *J. Geodesy*, vol. 80, no. 4, pp. 177–183, 2006.
[42] D. Hanley, A. S. D. D. Oliveira, X. Zhang, D. H. Kim, Y. Wei, and T. Bretl, "The impact of height on indoor positioning with magnetic fields," *IEEE Trans. Instrum. Meas.*, vol. 70, pp. 1–19, 2021.
[43] S.-C. Yeh, W.-H. Hsu, W.-Y. Lin, and Y.-F. Wu, "Study on an indoor positioning system using Earth's magnetic field," *IEEE Trans. Instrum. Meas.*, vol. 69, no. 3, pp. 865–872, Mar. 2019.
[44] H. Xie, T. Gu, X. Tao, H. Ye, and J. Lu, "A reliability-augmented particle filter for magnetic fingerprinting based indoor localization on smartphone," *IEEE Trans. Mobile Comput.*, vol. 15, no. 8, pp. 1877–1892, Aug. 2015.
[45] M. Sun, Y. Wang, S. Xu, H. Cao, and M. Si, "Indoor positioning integrating PDR/geomagnetic positioning based on the genetic-particle filter," *Appl. Sci.*, vol. 10, no. 2, p. 668, Jan. 2020.
[46] K. Qiu, H. Huang, W. Li, and D. Luo, "Indoor geomagnetic positioning based on a joint algorithm of particle filter and dynamic time warp," in *Proc. Ubiquitous Positioning, Indoor Navigat. Location-Based Services (UPINLBS)*, 2018, pp. 1–7.
[47] G. Wang, X. Wang, J. Nie, and L. Lin, "Magnetic-based indoor localization using smartphone via a fusion algorithm," *IEEE Sensors J.*, vol. 19, no. 15, pp. 6477–6485, Aug. 2019.
[48] R. Putta, M. Misra, and D. Kapoor, "Smartphone based indoor tracking using magnetic and indoor maps," in *Proc. IEEE 10th Int. Conf. Intell. Sensors, Sensor Netw. Inf. Process. (ISSNIP)*, Apr. 2015, pp. 1–6.
[49] C. Zhang, K. P. Subbu, J. Luo, and J. Wu, "GROPING: Geomagnetism and crowdsensing powered indoor navigation," *IEEE Trans. Mobile Comput.*, vol. 14, no. 2, pp. 387–400, Feb. 2014.
[50] W. Shao et al., "Location fingerprint extraction for magnetic field magnitude based indoor positioning," *J. Sensors*, vol. 2016, Dec. 2016, Art. no. 1945695.
[51] T. Michel, P. Geneves, H. Fourati, and N. Layaida, "On attitude estimation with smartphones," in *Proc. IEEE Int. Conf. Pervasive Comput. Commun. (PerCom)*, Mar. 2017, pp. 267–275.

Jian Kuang received the B.Eng. and Ph.D. degrees in geodesy and survey engineering from Wuhan University, Wuhan, China, in 2013 and 2019, respectively.

He is currently a Post-Doctoral Fellow with the GNSS Research Center, Wuhan University. His research interests include inertial navigation, pedestrian navigation, and indoor positioning.

Taiyu Li received the B.Eng. degree in geodesy and survey engineering from the China University of Mining and Technology, Xuzhou, China, in 2019. He is currently pursuing the master's degree with the GNSS Research Center, Wuhan University, Wuhan, China.

His research interests include pedestrian navigation and indoor positioning.

Qijin Chen received the B.Eng. and Ph.D. degrees in geodesy and survey engineering from Wuhan University, Wuhan, China, in 2011 and 2016, respectively.

He is currently an Associate Research Fellow with the GNSS Research Center, Wuhan University. His research interests include inertial navigation system (INS) and its applications in geodesy and precise surveying engineering, including railway track geometry measurements and underground pipeline surveying.

Baoding Zhou received the Ph.D. degree in photogrammetry and remote sensing from Wuhan University, Wuhan, China, in 2015.

He is currently an Assistant Professor with the College of Civil and Transportation Engineering, Shenzhen University, Shenzhen, China. His research interests include indoor localization and mapping, mobile computing, and intelligent transportation.

Xiaoji Niu received the B.Eng. degree in mechanical and electrical engineering and the Ph.D. degree from Tsinghua University, Beijing, China, in 1997 and 2002, respectively.

He was a Post-Doctoral Fellow with the Department of Geomatics Engineering, University of Calgary, Calgary, AB, Canada. He also worked as a Senior Scientist at the Advanced Technologies Group, SiRF Technology Inc., Shanghai, China. He is currently a Professor with the GNSS Research Center, Wuhan University, Wuhan, China. His research interests include global navigation satellite system (GNSS)/inertial navigation system (INS) integration and indoor navigation.